Control of Fuel Cell Breathing: Initial Results on the Oxygen Starvation Problem

Jay T. Pukrushpan, Anna G. Stefanopoulou, Huei Peng
University of Michigan, Ann Arbor

Abstract

In this paper we present the results of the air supply control problem for a Fuel Cell Stack (FCS) power system. In particular, we control the compressor motor in order to regulate (and replenish) the oxygen depleted from the fuel cell cathode during power generation. This task needs to be achieved rapidly and efficiently to avoid oxygen starvation and degradation of the stack voltage. Different control configurations and FCS measurements for feedback design are considered and their relative merits are analyzed. The tradeoff between reduction of oxygen starvation and fast net FCS power response during rapid current (load) demands is also delineated. We demonstrate that simple control techniques can provide useful insights and contribute to the design and development of fuel cell systems.

I. INTRODUCTION

Proton Exchange Membrane (PEM) Fuel Cells (FC) consist of a proton conducting membrane sandwiched between two platinum impregnated porous electrodes (membrane electrode assembly, MEA) as shown in Figure 1. Hydrogen molecules are split into protons and free electrons at the anode catalyst. The protons diffuse through the membrane to the cathode and react with the supplied oxygen and the returning electrons to produce water. During this process, the electrons pass through an external load circuit and provide useful electric energy. A typical PEM-FC provides up to 0.6 W/cm^2 depending on the catalyst loading, the membrane and electrode material, and the reactant (oxygen, O_2, and hydrogen, H_2) concentration in the anode and cathode. To satisfy different power requirements many fuel cells are connected electrically in-series to form a fuel cell stack (FCS).
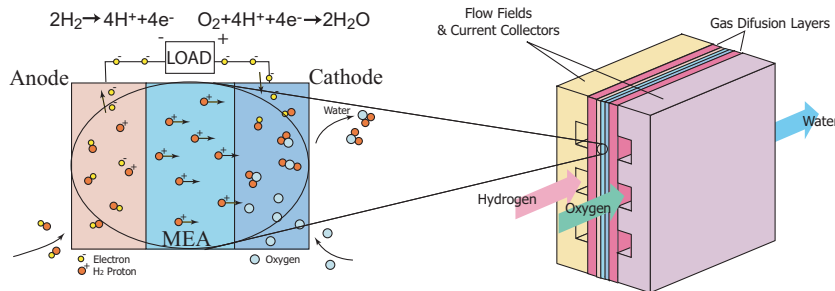

Fig. 1. *PEM Fuel Cell reactions and structure*

The fuel cell concept dates back to the early 1800s. It was first published in [33] and its invention has largely been attributed to W. R. Grove [16]. The availability and abundance of fossil fuel [18] limited interest in fuel cells as a power source. Recent advances in the power electronics area and efficient electric motors have sparked interest in direct electricity generation of the FC. Other major breakthrough include the development of (i) membrane structures with high conductivity, mechanical and electrochemical stability, and (ii) electrodes with high gas diffusivity and reduced usage of noble metal catalysts. In particular, Proton Exchange Membrane Fuel Cells (PEM-FC, also known as Polymer Electrolyte Membrane Fuel Cells) are considered by many to be in a relatively more advanced stage than other FC technologies. They have high power density, solid electrolyte, long cell and stack life, and low corrosion. They also operate at low temperatures (50-100 degree

Celsius), thus allowing for fast start-up. The dependency of PEM on high purity hydrogen reactant requires novel hydrogen generation and storage mechanisms. Fuel processors that reform hydrocarbon fuel to gas rich in hydrogen are currently considered as a near-term solution [3] to the hydrogen generation problem. Controlling fuel processors to provide hydrogen on demand [30], [37] can mitigate problems associated with hydrogen storage and distribution. In the long term, a hydrogen generation and distribution infrastructure based on renewable energy from wind, water, and sun, or reformed hydrocarbon fuel will help reduce our dependency on fossil fuels.

Compared to batteries, fuel cells provide higher energy density. For example, a methanol FC powertrain has an energy density around 1900 Wh/kg, whereas, a lead acid battery provides 40 Wh/kg [31]. Moreover battery recharging is more challenging and time consuming than refueling fuel cell vehicles with hydrogen or liquid fuel. Fuel Cells have higher efficiencies when compared to heat engines and their use in modular electricity generator and propulsion of electric vehicles is promising [19]. Fuel cell efficiency is high at partial loads which correspond to the majority of urban and highway driving scenarios [25]. At a nominal driving speed (30 mph) the efficiency of a FC electric drive using direct hydrogen from natural gas is two times higher than that of a conventional IC engine [31]. Using pure hydrogen as fuel can eliminate local emissions problems in densely populated urban environments.

The principle of electricity generation from a PEM-FC is very straightforward if the correct material properties, cell structure, and hydrogen are in place. The FC power response, however, is limited by the air flow and pressure regulation, and heat and water management [1]. As current is instantaneously drawn from the load source connected to the FC, the FC control system is required to maintain optimal temperature, membrane hydration, and partial pressure of the reactants across the membrane in order to avoid detrimental degradation of the FC voltage, and thus, efficiency reduction. These critical FC parameters must be controlled for a wide range of current, and thus power, by a series of actuators such as valves, pumps, compressor motors, expander vanes, fan motors, humidifiers and condensers. The resulting auxiliary actuator system, shown in Figure 2, is needed to make fine and fast adjustments to satisfy performance, safety and reliability standards that are independent of age and operating conditions. These requirements create challenging spatial and temporal control problems [39]. In this paper we assume compressed hydrogen is available and concentrate on the challenges associated with the temporal characteristics of the air (oxygen) supply. The overall FC system with the specific variables that we consider later in this paper are shown in Figure 2.
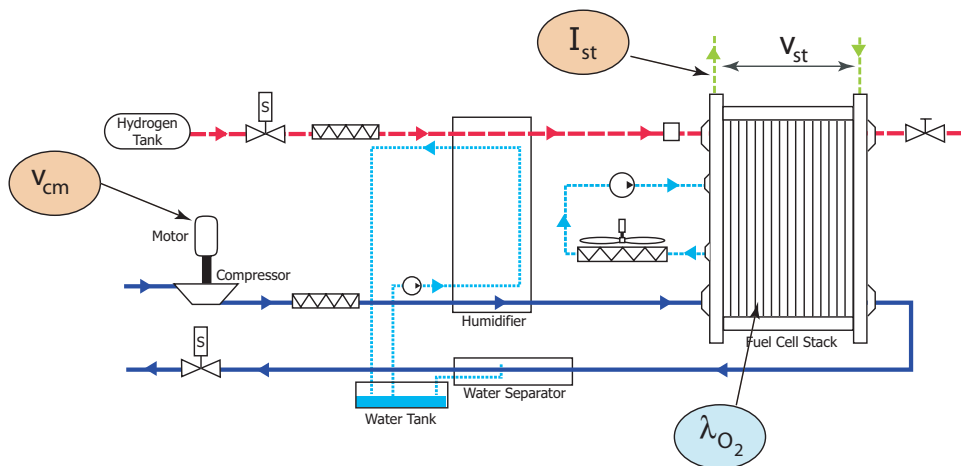

Fig. 2. Fuel cell system showing the major control subsystems and the control inputs and outputs that are discussed in following sections

We use model-based control design techniques based on a dynamic model developed in [29], [28] and summarized in Section III. A similar modeling approach is presented in [17] and discussed in [23], [26]. In this paper the stack terminal voltage, V_{st} is calculated based on dynamically evolving fuel cell load current and fuel cell operating conditions such as hydrogen and oxygen partial pressure. The physical parameters are calibrated based on data reported in literature and the system is sized to represent a high pressure FC

stack used in the Ford P2000 Fuel Cell vehicle [1]. The model is then used to analyze and design an air flow controller for the FC stack supercharging device that allows fast and robust air flow supply to the cathode.

This air flow needs to be controlled rapidly and efficiently to avoid oxygen starvation and extend the life of the stack [39] while minimizing the parasitic losses of the compressor [6]. Oxygen starvation is a complicated phenomenon that occurs when the partial pressure of oxygen falls below a critical level at any possible location within the meander of the air stream in the cathode [34]. It can be observed by a rapid decrease in cell voltage which in severe cases can cause a hot spot on the surface of a membrane cell. Before this catastrophic event happens, the stack diagnostic system that monitors individual cell voltage removes the current from the stack or triggers "shut-down." Although the phenomenon is spatially varying, it is largely believed that it can be avoided by regulating the excess oxygen ratio in the cathode, λ_{O_2}, which is a lumped (spatially invariant) variable.

II. Overview and Summary of Results

We control the air supply system for a high-pressure direct hydrogen FCS system using compressor motor voltage v_{cm}. The objective is to quickly and efficiently replenish the cathode oxygen depleted during step changes in current I_{st} drawn from the FCS. We achieve this by indirectly regulating the oxygen excess ratio λ_{O_2} in the FCS cathode.

Given that the exogenous input (stack current, I_{st}) is measured, a dynamic feedforward controller that cancels the effect of current to oxygen excess ratio is theoretically feasible. The design of such an ideal "cancellation" controller is based on inverting the linearized plant model in Section VI. However, as shown in Figure 2, the variables manipulated via the actuator v_{cm} are upstream of where the disturbance I_{st} affects the performance variable λ_{O_2}. This topology of actuated and performance variables limits the disturbance rejection capabilities of any realizable feedforward controller. In Section VII, a two Degrees Of Freedom (2DOF) controller is designed based on a static feedforward and an integral observer-based output feedback controller. The challenge here arises from the fact that all the traditionally used measurements for λ_{O_2} regulation are upstream of the performance variable due to difficulties in sensing within a vapor saturated flow stream.

Apart from the design of the 2DOF controller, we also provide three additional results: First, in Section VII-B we demonstrate that the FCS voltage increases the system observability and thus enables a higher gain controller that improves transient λ_{O_2} regulation and robustness significantly. Currently, voltage is used in diagnostic and emergency shut-down procedures due to its fast reaction to oxygen starvation, but we clearly demonstrate its usefulness and use in a feedback design. Note here that the FCS voltage cannot be used as the sole output injection in the FCS observer because it depends on many other variables such as hydrogen starvation [4], [30], membrane humidification (dryness and flooding). In hindsight of our results, the FCS voltage provides a natural indication of oxygen starvation, and thus, should be used in coordination with other feedback measurements for the air controller.

Our second result is the characterization of the closed loop FCS (FCS+air controller) impedance. Specifically, we show in Section VIII that the closed loop fuel cell impedance resembles a passive resistive power source ($R_{st} = 0.05 \ \Omega$) for current excitations slower than 0.3 rad/sec. The FCS is viewed as a power source from the power electronics when connected to a traction motor or to a grid of heterogeneous power sources [21], [32]. Its impedance defines the "power quality" of the FCS as a power source [21]. Many studies thus far [36] have used a static polarization curve for the Voltage-to-Current relation, which assumes a perfect or a non-existent FCS reactant flow controller.

Finally, in Section IX we show that minimizing the FCS system parasitic losses and providing fast air flow regulation are conflicting objectives. The conflict arises from the fact that the supercharger is using part of the stack power to accelerate. One way to resolve this conflict is to augment the FCS system with an auxiliary battery or an ultracapacitor that can drive the auxiliary devices or can potentially buffer the FCS from transient current demands. These additional components, however, will introduce complexity and additional weight that might not be necessary [31]. We analyze the tradeoff between the two objectives using a Single-Input Two-Output (SITO) control configuration [14]. We then show that a compromise needs to be made between oxygen starvation and FCS net power for transients faster than 0.7 rad/sec (see Figure 21).

Although this answer is specific to our system, our analysis procedure is general and can be applied to other fuel cell systems.

III. Nonlinear Fuel Cell Stack System Model

A nonlinear dynamic model of the fuel cell system is developed using electrochemical, thermodynamic and zero-dimensional fluid flow principles. We concentrate on the dynamical PEM-FC behavior associated with the reactant pressure and flow and we neglect the slower dynamics associated with temperature regulation and heat dissipation. We thus assume a well regulated averaged stack temperature, T_{st}, throughout our modeling, analysis, and control design. We also assume that the inlet reactant flows in the cathode and anode can be humidified in a consistent and rapid way. Although the last assumption will not be satisfied in practice, especially during fast transients, lack of experimental data prevents the accurate representation and analysis of dynamic coupling between temperature and humidity variations.

The volume associated with the fuel cell system is shown in Figure 3. In this study, it is assumed that the multiple cathode and anode volumes of fuel cells in the fuel cell stack are lumped together as a single stack cathode and anode volume. Pressurized hydrogen is supplied to the FC stack anode through a pressure regulator that we discuss in Section III-B. The anode supply or return manifold volumes are very small and the pure hydrogen flow allows us to lump all these volumes to one "anode" volume. We denote all the variables associated with the lumped anode volume with a subscript (an). On the other hand, the cathode supply manifold (sm) lumps all the volumes associated with pipes and connection between the compressor and the stack cathode (ca). The cathode supply manifold volume in the Ford P2000 experimental vehicle is significant due to the large distance between the flow control device (located in the front of the vehicle) and the stack (located in the rear trunk of the vehicle) [1]. The cathode return manifold is small and represents the lump volume of pipes downstream of the stack cathode.
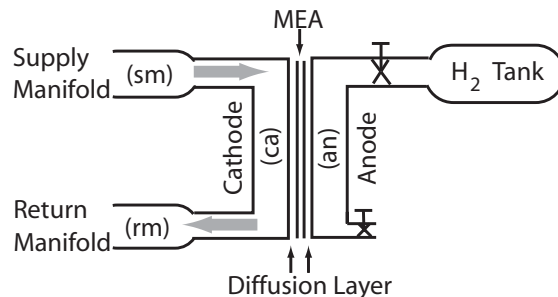

Fig. 3. *Volumes in fuel cell reactant supply system*

Masses (kg) are denoted with m, mass flows (kg/s) with W, molar masses (kg/mol) with M, pressure (kPa) with p, temperatures (K) with T, vapor saturation pressure at temperature T_x with $p_{sat}(T_x) = p_{sat}^x$, relative humidity with ϕ, humidity ratio with Ω, rotational speed (rad/s) with ω, power (Watts) with P, current (A) with I, current density (A/cm^2) with i, area (cm^2) with A, volume (m^3) with V, voltage (Volts) with v. The variables associated with vapor are denoted with a subscript v, water with w, oxygen with O_2, nitrogen with N_2, hydrogen with H_2. The variables in specific volumes have as a second subscript the volume identifier (sm, ca, rm, an). The variables associated with the electrochemical reactions are denoted with rct. The variables for the compressor or the compressor motor have cp or cm, respectively, as their subscript. Similarly, the stack variables use st, the individual fuel cells variables use fc, the atmospheric variables use atm, and the membrane variables use mbr.

A. State Space Representation

Mass conservation is used to obtain governing equations for oxygen, nitrogen and water mass inside the cathode volume:

$$\frac{dm_{O_2}}{dt} = W_{O_2,in} - W_{O_2,out} - W_{O_2,rct} \tag{1}$$

$$\frac{dm_{N_2}}{dt} = W_{N_2,in} - W_{N_2,out} \tag{2}$$

$$\frac{dm_{w,ca}}{dt} = W_{v,ca,in} - W_{v,ca,out} + W_{v,gen} + W_{v,mbr}. \tag{3}$$

Note that the rate of change of the mass of water inside the cathode, $m_{w,ca}$ depends solely on the summation of vapor flows, because it is assumed that the liquid water does not leave the stack and evaporates into the cathode gas if cathode humidity drops below 100%. The mass of water is in vapor form until the relative humidity of the gas exceeds saturation (100%), the point at which vapor condenses into liquid water. The cathode pressure is then calculated using Dalton's law of partial pressures ($p_{ca} = p_{O_2} + p_{N_2} + p_{v,ca}$). Note also that the partial pressures for the oxygen ($p_{O_2} = \frac{RT_{st}}{M_{O_2}V_{ca}}m_{O_2}$), nitrogen ($p_{N_2} = \frac{RT_{st}}{M_{N_2}V_{ca}}m_{N_2}$) and vapor ($p_{v,ca} = \phi_{ca}p_{sat}^{st}$) in the cathode are algebraic functions of the states through the ideal gas law and the psychrometric laws since the cathode temperature is considered fixed and equal to the overall stack temperature at $T_{st} = 353$ K ($80°C$). Given the vapor saturation pressure p_{sat}^{st}, the relative humidity is $\phi_{ca} = \min\left[1, \frac{m_{w,ca}RT_{st}}{p_{sat}^{st}M_vV_{ca}}\right]$.

The flow rates in and out of the cathode are defined based on the difference between the pressure of the upstream and downstream gas. These relations are defined in the next section based on the states in the supply and the return manifold. In particular, the rate of change of mass inside the supply manifold, m_{sm}, is governed by the mass conservation principle and the rate of change of supply manifold pressure, p_{sm}, is governed by the energy conservation principle:

$$\frac{dm_{sm}}{dt} = W_{cp} - W_{sm} \tag{4}$$

$$\frac{dp_{sm}}{dt} = \frac{\gamma R}{M_a^{atm}V_{sm}}(W_{cp}T_{cp} - W_{sm}T_{sm}) \tag{5}$$

where R is the universal gas constant and M_a^{atm} is the molar mass of atmospheric air at ϕ_{atm}, V_{sm} is the manifold volume and $T_{sm} = \frac{p_{sm}V_{sm}M_a^{atm}}{Rm_{sm}}$ is the supply manifold gas temperature.

The flow and temperature out of the compressor (W_{cp} and T_{cp}) depend on the compressor rotational speed ω_{cp} that is governed by the combined compressor motor inertia, J_{cp},

$$J_{cp}\frac{d\omega_{cp}}{dt} = \frac{1}{\omega_{cp}}(P_{cm} - P_{cp}) \tag{6}$$

where P_{cm} and P_{cp} are the powers supplied to the compressor motor and power required to drive the compressor, respectively. The compressor motor power, $P_{cm}(v_{cm}, \omega_{cp})$, is calculated from the motor input voltage, v_{cm} that is the actuator signal. Other nonlinear maps are used to calculate the consumed compressor power $P_{cp}(\omega_{cp}, \frac{p_{sm}}{p_{atm}}, T_{atm})$, the flow rate $W_{cp}(\omega_{cp}, \frac{p_{sm}}{p_{atm}}, T_{atm})$ and flow temperature $T_{cp}(\omega_{cp}, \frac{p_{sm}}{p_{atm}}, T_{atm})$. Exact numerical values for all these nonlinear maps can be found in [27].

The state equation of the return manifold pressure is

$$\frac{dp_{rm}}{dt} = \frac{RT_{st}}{M_a^{ca}V_{rm}}(W_{ca} - W_{rm}). \tag{7}$$

where V_{rm} and T_{st} is return manifold volume and gas temperature, respectively. Note that the isothermal assumption in the return manifold allows us to eliminate the state m_{rm} that now depends on p_{rm} based on the ideal gas law ($m_{rm} = \frac{p_{rm}V_{rm}M_a^{ca}}{RT_{st}}$).

The governing equations for hydrogen and water in the anode can be written as

$$\frac{dm_{H_2}}{dt} = W_{H_2,in} - W_{H_2,purge} - W_{H_2,rct} \tag{8}$$

$$\frac{dm_{w,an}}{dt} = W_{v,an,in} - W_{v,purge} - W_{v,mbr} \tag{9}$$

with the anode pressure and relative humidity calculated as

$$p_{an} = \underbrace{\frac{RT_{st}}{M_{H_2}V_{an}}m_{H_2}}_{p_{H_2}} + \underbrace{\min\left[1, \frac{RT_{st}m_{w,an}}{M_v V_{an} p_{sat}^{st}}\right]}_{\phi_{an}} p_{sat}^{st}.$$

In summary, the nonlinear model based on the state equations (1)-(9) contains nine states which are

$$x_{NL} = \left[m_{O_2}, m_{H_2}, m_{N_2}, \omega_{cp}, p_{sm}, m_{sm}, m_{w,an}, m_{w,ca}, p_{rm}\right]^T.$$

B. Reactant Flow Rates

The air temperature in the supply manifold T_{sm} from Eq. (4)-(5) is typically higher than the desired air inlet temperature T_{st} due to the high exit temperature from the compressor, T_{cp}. We assume then a "perfect" heat exchanger that regulates the temperature of the cathode inlet-flow to the desired T_{st}. Similarly, we assume an "instantaneous" humidifier that regulates the relative humidity of the cathode inlet-flow to the desired $\phi_{ca,in}^{des}$ by injecting vapor. We employ these assumptions despite their severity, in order to achieve some basic understanding of the oxygen starvation problem by isolating the flow/pressure dynamics from the temperature and humidity dynamics. In future work we can extend the model to include realistic heat exchanger and vaporizer characteristics or allow a varying $\phi_{ca,in} \neq \phi_{ca,in}^{des}$ and $T_{ca,in} \neq T_{st}$ and assess the controller performance.

The outlet mass flow rates of the supply manifold $W_{sm}(p_{ca}, p_{sm}, T_{sm})$, the cathode $W_{ca}(p_{rm}, p_{ca}, T_{st})$, and the return manifold $W_{rm}(p_{atm}, p_{rm}, T_{st})$ are calculated using nozzle equations [29].

Based on the gas out of the supply manifold, and specifically, its mass flow rate W_{sm} and pressure p_{sm}, its desired humidity $\phi_{ca,in}^{des}$ and temperature T_{st} and the atmospheric air conditions ($p_{atm}, T_{atm}, \phi_{atm}, \chi_{O_2}$) we calculate the individual species of Eq. (1)-(3):

$$W_{O_2,in} = y_{O_2}\frac{1}{1+\Omega_{atm}}W_{sm} \tag{10}$$

$$W_{N_2,in} = y_{N_2}\frac{1}{1+\Omega_{atm}}W_{sm} \tag{11}$$

$$W_{v,ca,in} = \frac{\Omega_{ca,in}}{1+\Omega_{atm}}W_{sm} \tag{12}$$

We define the mass fraction of oxygen and nitrogen in the dry atmospheric air as $y_{O_2} = \chi_{O_2}M_{O_2}/M_a^{atm}$ and $y_{N_2} = (1-\chi_{O_2})M_{N_2}/M_a^{atm}$, where $M_a^{atm} = \chi_{O_2}M_{O_2} + (1-\chi_{O_2})M_{N_2}$ and $\chi_{O_2} = 0.21$ is the oxygen mole fraction in dry air. The atmospheric (at compressor inlet) and cathode inlet humidity ratio are given by:

$$\Omega_{atm} = \frac{M_v}{M_a}\frac{\phi_{atm}p_{sat}^{atm}/p_{atm}}{1-\phi_{atm}p_{sat}^{atm}/p_{atm}} \tag{13}$$

$$\Omega_{ca,in} = \frac{M_v}{M_a}\frac{\phi_{ca,in}^{des}p_{sat}^{st}}{p_{sm}(1-\phi_{atm}p_{sat}^{atm}/p_{atm})} \tag{14}$$

Also, the mass flow rate of each species out of the cathode is calculated as:

$$W_{O_2,out} = \frac{m_{O_2}}{m_{ca}}W_{ca} \tag{15}$$

$$W_{N_2,in} = \frac{m_{N_2}}{m_{ca}}W_{ca} \tag{16}$$

$$W_{v,ca,out} = \frac{p_{v,ca}V_{ca}M_v}{RT_{st}m_{ca}}W_{ca}. \tag{17}$$

where $m_{ca} = m_{O_2} + m_{N_2} + \frac{p_{v,ca}V_{ca}M_v}{RT_{st}}$ is the total mass of the cathode gas.

The rates of oxygen reacted, $W_{O_2,rct}$, hydrogen reacted, $W_{H_2,rct}$, and water generated $W_{v,gen}$, in the fuel cell reaction are calculated from the stack current, I_{st}, using the electrochemical equations

$$W_{O_2,rct} = M_{O_2}\frac{nI_{st}}{4F} \tag{18}$$

$$W_{H_2,rct} = M_{H_2}\frac{nI_{st}}{2F} \tag{19}$$

$$W_{v,gen} = M_v\frac{nI_{st}}{2F} \tag{20}$$

where n is the number of cells in the stack and F is the Faraday number ($F = 96485$ Coulombs).

The mass flow of vapor across the membrane, $W_{v,membr}$, is calculated using mass transport principles and membrane properties given in [35]:

$$W_{v,membr} = M_v A_{fc} n \left(n_d \frac{i}{F} - D_w \frac{(\phi_{ca} - \phi_{an})}{t_m} \right) \tag{21}$$

where A_{fc} is the active area of the fuel cell and i is the fuel cell current density (current per active area, I_{st}/A_{fc}). Variable $n_d(\phi_{ca}, \phi_{an})$ is the electro-osmotic coefficient, $D_w(\phi_{ca}, \phi_{an}, T_{st})$ is the diffusion coefficient, and t_m is membrane thickness used in the work of [35], [22] and documented in [29].

The anode inlet flow rate, $W_{an,in} = k_{p,an}(p_{ca} - p_{an} + \delta p)$, is regulated to maintain a constant pressure difference δp across the membrane. This can be achieved by using a high-gain proportional control with reference signal from the supply manifold pressure sensor. The hydrogen and water flows to the anode in Eq (8)-(9) are calculated by

$$W_{H_2,in} = \frac{1}{1 + \Omega_{an,in}}W_{an,in} \tag{22}$$

$$W_{v,an,in} = \frac{\Omega_{an,in}}{1 + \Omega_{an,in}}W_{an,in} \tag{23}$$

The anode inlet humidity ratio, $\Omega_{an,in}$, is calculated from the flow temperature, $T_{an,in}$, relative humidity, $\phi_{an,in}$, and pressure, $p_{an,in}$ of the flow leaving the hydrogen humidifier:

$$\Omega_{an,in} = \frac{M_v}{M_{H_2}} \frac{\phi_{an,in}p_{sat}^{an,in}}{p_{an,in}}. \tag{24}$$

The $\phi_{an,in}$ is set to 50% in this study because it results in sub-saturated conditions in the anode ($\phi_{an} < 1$), which in-turn prevents anode flooding. The anode purge is, thus, disabled, i.e., $W_{v,purge} = 0$.

C. Performance Variables

In this paper the compressor motor voltage, v_{cm}, is controlled during rapid changes in the current, I_{st}, drawn from the FCS that is described by the nonlinear state equations in (10):

$$\begin{aligned} \dot{x}_{NL} &= f(x_{NL}, u, w) &&\text{State Equations} \\ u &= v_{cm} &&\text{Actuator (Control) Signals} \\ w &= I_{st} &&\text{Exogenous Inputs} \end{aligned}$$

The current is considered as an exogenous input or disturbance to the system. The performance variables are the net power produced by the FCS system, $P_{net} = P_{net}^{ref}(I_{st})$, and the excess oxygen ratio in the FCS cathode, $\lambda_{O_2} = \lambda_{O_2}^d$. Both performance variables are defined below.

The fuel cell voltage v_{fc} is given in the form of polarization curves or a nonlinear map [29] of current density, i, and other anode and cathode variables, i.e., $v_{fc}(i, p_{O_2}, p_{H_2}, T_{st}, \phi_{ca}, \phi_{an})$. Many fuel cells are connected in series to form a Fuel Cell Stack (FCS), hence, the total FCS voltage and power are $v_{st} = n v_{fc}$ and $P_{st} = n A_{fc} v_{fc} i$. The air compressor is a major contributor of parasitic loss in the fuel cell system [6]. Therefore, the net power obtained from the fuel cell stack system is

$$P_{net} = P_{st}(x_{NL}, I_{st}) - P_{cm}(x_{NL}, v_{cm}), \tag{25}$$

where we use the notation $(x_{NL}, \bullet)$ to denote nonlinear dependency on states and inputs.
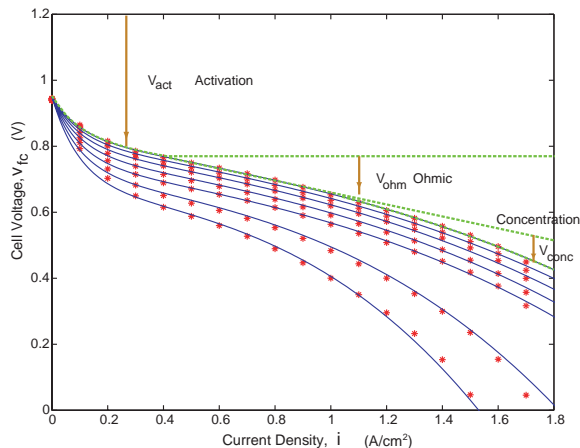

Fig. 4. Fuel cell polarization curve for different oxygen partial pressures p_{O_2}

Figure 4 shows that low oxygen partial pressure p_{O_2} decreases the fuel cell voltage and thus FCS system power. In our model we neglect the variations in the spatial distribution of composition in the cathode flow field that allow the transportation of oxygen-rich reactants to the fuel cell and removal of the oxygen-depleted air. We assume homogeneous oxygen concentration throughout the cathode flow field and we model the cathode as a lumped volume with manifold filling and emptying dynamics in Eq. (1).

The oxygen excess ratio λ_{O_2} is then used as the lumped (spatially invariant) variable that indicates FCS oxygen starvation:

$$\lambda_{O_2} = \frac{W_{O_2, in}(x_{NL})}{W_{O_2, rct}(x_{NL}, I_{st})} \tag{26}$$

based on Eq. (10) and (18). Again, we explicitly denote the dependency on the input I_{st} that directly affects $W_{O_2, rct}$ and causes instantaneous drop of λ_{O_2}. On the other hand, the actuator v_{cm} affects the λ_{O_2} indirectly through the states x_{NL}.

High λ_{O_2}, and thus high oxygen partial pressure, improves the total and the net FCS power, P_{st} and P_{net} respectively. However, above an optimum λ_{O_2} level, further increase will cause excessive increase of P_{cm} and thus it will cause decrease of P_{net}. For different current I_{st} drawn from the FCS there is an optimum λ_{O_2} (see [29]). For simplification we assume for now a fixed $\lambda_{O_2}^d = 2$. In the future, extremum seeking or other maximum-finding techniques can be used to search on-line for the optimum excess oxygen ratio levels.

The combined control design objective is to define the compressor motor input voltage, v_{cm}, in order to maintain $\lambda_{O_2} = 2$ and achieve the desired fuel cell system net power that can be calculated based on a static map of the current drawn from the FCS, $P_{net} = P_{net}^{ref}(I_{st})$. The potential measurements include air flow rate through the compressor, W_{cp}, supply manifold pressure, p_{sm}, and stack voltage, v_{st}. The resulting control

problem is shown in Figure 5 and defined as follows:

$$y = [W_{cp}\ p_{sm}\ v_{st}]^T = h_y(x_{N_L}, u, w) \quad \text{Measurements}$$
$$z = [e_{P_{net}}\ \lambda_{O_2}]^T = h_z(x_{N_L}, u, w) \quad \text{Performance Variables}$$

where $e_{P_{net}}$ is defined as the difference between the desired and the actual system net power, i.e., $e_{P_{net}} = P_{net}^{ref} - P_{net}$.
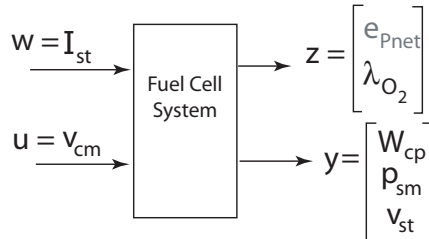

Fig. 5.   Control problem formulation

Figure 2 illustrates the physical location of all the input/output control variables. We formulate two control objectives $e_{P_{net}}^d = 0$ and $\lambda_{O_2}^d = 2$, but focus on the problem of using the compressor motor voltage, v_{cm}, to regulate the oxygen excess ratio $\lambda_{O_2}^d = 2$ in the first sections of this paper. Note that the two objectives are both achievable at steady-state, but their transients are considerably different, and thus, cannot be achieved simultaneously by a single control actuator. The objective of achieving the desired transient system net power is ignored in the first part of this paper, which represents the case where the power management system can rely on a secondary power source such as a battery. The tradeoff between the two performance variables, i.e., $e_{P_{net}}$ and λ_{O_2}, is discussed in Section IX of this paper.

IV. Control Configurations

We consider three different control schemes for the fuel cell stack system as illustrated in Figure 6. Because the current that acts as a disturbance can be measured, a static function that correlates the steady-state value between the control input, v_{cm}, and the disturbance, I_{st}, could be used in the feedforward path. This static feedforward shown in Figure 6(a), denoted from now on as "sFF", is easily implemented with a look-up table. The calculation of the static feedforward controller is based on finding the compressor voltage command, v_{cm}^*, that achieves the air flow that replenishes the oxygen flow depleted during a current command, I_{st}. For specific ambient conditions (pressure, temperature, and humidity), the required air flow can be calculated analytically from the stack current, $W_{cp}^* = f_{cp}(I_{st})$, based on electrochemical and thermodynamic principles:

$$W_{cp}^* = (1 + \Omega_{atm})\, W_{air}^*$$
$$= \left(1 + \frac{M_v}{M_a^{atm}} \frac{\phi_{atm} p_{sat}^{atm}}{(p_{atm} - \phi_{atm} p_{sat}^{atm})}\right) \frac{1}{\chi_{O_2}} \lambda_{O_2} M_{O_2} \frac{n I_{st}}{4F}. \tag{27}$$

The inversion of compressor and compressor motor maps to find $v_{cm}^* = f_{cm}(I_{st})$ that gives the desired air flow, W_{cp}^*, is not trivial but can be performed using a mathematical model or experimental testing. In this paper we use nonlinear simulations to determine the static feedforward controller from "w to u" that cancels the effect "w to z_2" at steady-state.

When a mathematical model of the FCS is available, a dynamic feedforward can be designed to achieve better transient response. In particular, a linear dynamic feedforward controller that cancels the effect of w to z_2 over a wide range of frequencies is designed in Section VI. This cancellation controller is based on the inversion of the linear plant and is denoted from now on as the "dFF" controller. A proportional integral feedback controller (PI) is designed and added on the "dFF" controller in order to reduce its sensitivity on modeling error, device aging, and variations in ambient conditions. As discussed in Section VI, the PI feedback controller has to be very slow so that the transient response of the combined dFF+PI does not deteriorate. The need for small integral gain arises from the fact that the PI controller acts on the compressor
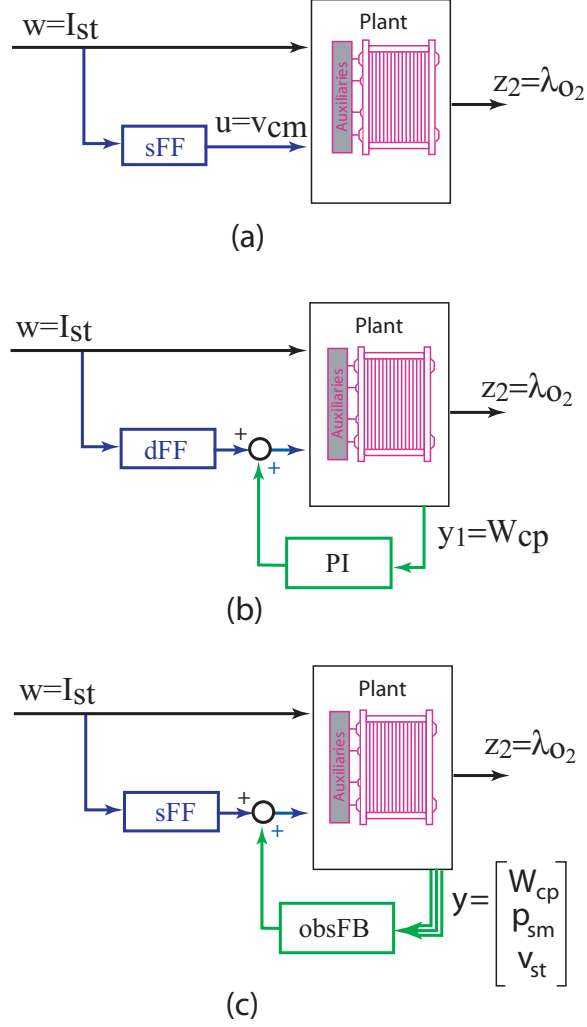
Fig. 6. Different control configurations

flow ($y_1 = W_{cp}$) that is upstream of the air flow at the cathode inlet (W_{sm}). Note that W_{sm} directly affects the performance variable $z_2 = \lambda_{O_2}$ through Eq. (10) and (26) but it is difficult to measure due to the high relative humidity in the cathode inlet conditions.

In Section VII we study the performance of high order (observer-based integral-augmented) feedback controllers. The feedback is combined with the static feedforward as shown in Figure 6(c) to form the "sFF+obsFB" controller that has similar order with the "dFF+PI" controller. We show that the observer-based feedback that uses only the air flow measurement ($y_1 = W_{cp}$) achieves only slightly higher closed loop bandwidth than the simple PI feedback controller. Significant improvement of the closed loop bandwidth is achieved by measuring the stack voltage and adding this signal to the observer-based feedback controller. The multiple measurements allow better observability of the system states (x), and consequently, the transient excess oxygen ratio $z_2 = \lambda_{O_2}$. We denote as "sFF+obsFB1" and as "sFF+obsFB3" the observer-based controller that depends on one (1) or three (3) measurements, respectively.

In summary, the sFF+obsFB3 controller has similar order and transient response with the dFF+PI but superior output sensitivity due to its high closed loop bandwidth. Indeed, the transient response of the dFF+PI is based on the dynamic feedforward term, whereas, the sFF+obsFB3 achieves its good transient response due to the fast feedback term.

V. Linearization

The LTI system analysis in the MATLAB/Simulink control system toolbox is used to linearize the nonlinear system that is developed in Section III. The nominal operating point is chosen where the system net power is $z_1^o = 40$ kW and oxygen excess ratio is $z_2^o = 2$. The inputs that correspond to this operating point are stack current at $w^o = 191$ A and compressor motor voltage at $u^o = f_{cm}(191) = 164$ V based on the static feedforward controller design discussed in the previous Section. We denote also the nominal states at the equilibrium of the system for nominal inputs w^o and u^o. The linear model includes the static feedforward controller (sFF) and is given by:

$$
\begin{aligned}
\delta \dot{x} &= A\delta x + B_u \delta u + B_w \delta w \\
\delta z &= C_z \delta x + D_{zu} \delta u + D_{zw} \delta w \\
\delta y &= C_y \delta x + D_{yu} \delta u + D_{yw} \delta w
\end{aligned}
\tag{28}
$$

where $\delta(\cdot) = (\cdot) - (\cdot)^o$ represents the deviation from the nominal value. The matrices are given in the Appendix. The state, x, measurements, y, performance variables, z, input, u, and disturbance, w, are

$$
\begin{aligned}
x^T &= \left[m_{O_2}, m_{H_2}, m_{N_2}, \omega_{cp}, p_{sm}, m_{sm}, m_{w,an}, p_{rm} \right] \\
y^T &= [W_{cp}, p_{sm}, v_{st}] \\
z^T &= [e_{Pnet}, \lambda_{O_2}] \\
u &= v_{cm} \\
w &= I_{st}
\end{aligned}
$$

Here, the units of states and outputs are scaled such that each variable has a comparable magnitude. The units are as follows: mass in grams, pressure in bar, rotational speed in kRPM, mass flow rate in g/sec, power in kW, voltage in V, and current in A.

Note that the resulting linear model has eight states while the nonlinear model has nine states. The state that is removed, because it is unobservable after linearization, is the mass of water in the cathode $m_{w,ca}$. The reason is as follows. With the parameters of the membrane water flow in Eq. (21), there is always excessive water flow from anode to cathode that results in fully humidified (vapor saturated) cathode gas. Thus, for constant temperature, the vapor pressure is constant and equal to the saturated vapor pressure. Our nonlinear model does not include the effects of liquid condensation, also known as "flooding," on any of the measured or performance variables. Typically flooding affects the FCS voltage, through a complex mechanism that is not well understood and thus not captured in our model. As a result, the cathode water mass is not observable from the specified outputs in the numerical linearization. On the other hand, the anode vapor pressure is observable and it is included in the linear model because variations in the FCS current affect the partial pressure of vapor in the anode that is always less than its saturated value. The change in vapor pressure affects the hydrogen partial pressure due to the fast P controller that regulates the anode pressure to be equal to the cathode pressure. The hydrogen pressure in turn affects the FCS voltage and makes the $m_{w,an}$ observable.

There are two linearization cases. The first is the regular input/output linearization of the plant shown in Figure 6(b) with $(A, B_u, B_w, \ldots, D_{zw})$ as in Eq. (28). This is used in the sequel section for the design of the dynamic feedforward. The resulting system matrices are given in Table II of Appendix. The second linearization is performed to include the static feedforward $f_{cp}(w)$ in addition to feedback control u_{fb} shown in Figure 6(c) $u = u_{fb} + u^* = u_{fb} + f_{cp}(w)$. The matrices $(A, B_u, B_w^o, \ldots, D_{zw}^o)$ are given in Table III in Appendix and are used in Section VII where the feedback controller is designed. As our notation indicates, the matrices of the two systems are the same, except $B_w^o = \left(\frac{\partial f}{\partial w} + \frac{\partial f}{\partial u} \frac{\partial f_{cp}}{\partial w} \right) |_{x^o, u^o, w^o} = B_w + B_u \frac{\partial f_{cp}}{\partial w} |_{w^o}$ and $D_{z_1 w}^o = D_{z_1 w} + D_{z_1 u} \frac{\partial f_{cp}}{\partial w} |_{w^o}$ matrices. Note that $D_{z_2 w}$ is the same for both cases because $D_{z_2 u} = 0$. For both linear systems, the anode flow control (proportional) is included in the linearization.

VI. Dynamic Feedforward

Due to the topology of the control variable, $u = v_{cm}$, and the disturbance, $w = I_{st}$, with respect to the performance variable, $z_2 = \lambda_{O_2}$, the disturbance rejection capabilities of the open loop system are moderate. In particular, the control signal, $u = v_{cm}$ affects performance variable $z_2 = \lambda_{O_2}$ through the dynamics associated with the compressor inertia, supply manifold filling, and eventually, cathode manifold filling (see also Figure 2 for the physical location of the control signal). On the other hand the disturbance, $w = I_{st}$, affects the performance variable $z_2 = \lambda_{O_2}$ directly (see Figure 2 and Eq. (26)). It is clear that in order to achieve good disturbance rejection the control variable, u, needs to use a lead filter of the measured disturbance, w (see [11]). The lead filter can be based on the inversion of the open loop dynamics from "u to z_2."

Using the linear model given in the Appendix, the system can be arranged in the transfer function form

$$\Delta Z_2 = G_{z2u}\Delta U + G_{z2w}\Delta W \tag{29}$$

where $G_{z2u} = C_{z_2}(sI - A)^{-1}B_u$ and $G_{z2w} = C_{z_2}(sI - A)^{-1}B_w + D_{z_2w}$, and all upper-case variables are in the Laplace domain. For simplicity, the Laplace variable "s" is not explicitly shown. Let a dynamic feedforward controller be $\Delta U = K_{uw}\Delta W$ as shown in Figure 7. The transfer function from W to Z_2 can be written as
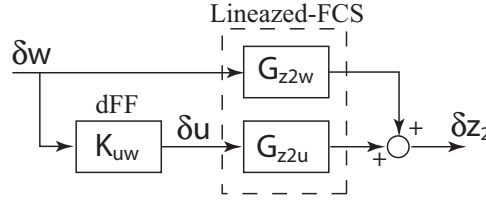

Fig. 7. Dynamic feedforward control

$$T_{z_2w} = \frac{\Delta Z_2}{\Delta W} = (G_{z2w} + G_{z2u}K_{uw}) \tag{30}$$

For complete disturbance rejection $T_{z_2w} = 0$ and K_{uw}^{ideal} cancels the response of z_2 due to w:

$$K_{uw}^{ideal} = -G_{z2u}^{-1}G_{z2w}. \tag{31}$$

The open loop plant dynamics G_{z2u} is minimum phase and G_{z2w} is stable, thus K_{uw}^{ideal} is a stable controller. Direct modification of the current disturbance or techniques from [5] and [9] are needed in the case of a delay or non-minimum phase system dynamics. The inversion of the G_{z2u} transfer function calculated in Eq. (31) is not proper and thus is not realizable. Moreover, K_{uw}^{ideal} corresponds to large amplitude of control input at high frequencies. To obtain a strictly proper feedforward controller, high-frequency components of K_{uw}^{ideal} are removed using a low pass filter, i.e.

$$K_{uw} = -\frac{1}{(1 + \frac{s}{\alpha_1})(1 + \frac{s}{\alpha_2})(1 + \frac{s}{\alpha_3})} \cdot G_{z2u}^{-1}G_{z2w} \tag{32}$$

The values of α_1, α_2, and α_3 used are, 80, 120, and 120, respectively. Figure 8 shows a comparison between K_{uw}^{ideal} and the strictly proper K_{uw}. By increasing the value of α's, the response of z_2 can be made faster at the expense of large control action.

Even though the dynamic feedforward cancels the effect of w to z_2 at a wide range of frequencies, the model-based inversion can adversely affect the disturbance rejection capability in the presence of unknown disturbance, modeling error, and parameter variation. Because there is no feedback, the sensitivity function of the system with respect to unknown disturbance is equal to unity at all frequencies. The frequency domain modifications in [8] can be used to reduce the cancellation controller sensitivity if one can find bounds on the size of the plant uncerainties. In this paper, we use instead a simple PI controller that reduces the closed
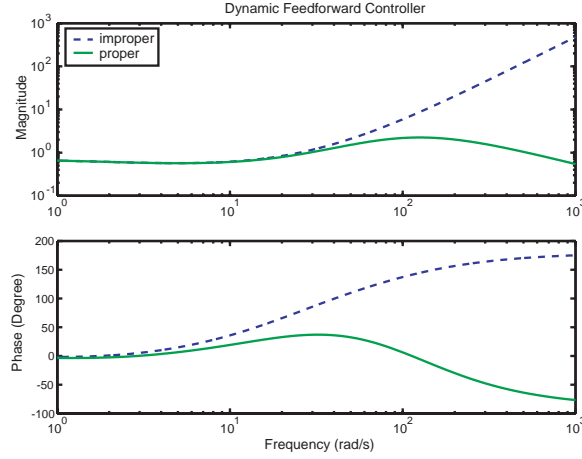
Fig. 8. Frequency plot of dynamic feedforward controller

loop sensitivity at low frequencies and ensures that W_{cp} reaches at steady state the desired $W_{cp}^* = f_{cp}(I_{st})$. The dFF+PI controller is given by:

$$u(t) = K_{uw}(I_{st}(t) - I_{st}^o) + k_{p,ca}(f_{cp}(I_{st}(t)) - W_{cp}(t)) + k_{I,ca} \int_0^t (f_{cp}(I_{st}(\tau)) - W_{cp}(\tau))d\tau \qquad (33)$$

We have observed that increasing weighting on the integrator degrades the speed of $z_2 = \lambda_{O_2}$ response. A small integral gain $k_{I,ca}$ is thus used. The fundamental reason that increasing integral gain degrades the response of performance variable $z_2 = \lambda_{O_2}$ is because the integrator is applied to the air flow measurement $y_1 = W_{cp}$ far upstream from the position where $z_2 = \lambda_{O_2}$ is defined (see Figure 2). Thus, moving the flow measurement to the position closer to the fuel cell stack (either flow entering or exiting) is more appropriate in terms of designing integral control. However, in practice, flow measurement near the stack is problematic due to high vapor concentration and potential condensation on the sensor [15]. Moreover, due to the large change in the thermodynamic condition of the flow at this location, it is impossible to accurately calculate the required amount of air flow to be used as a reference value in the integral control.
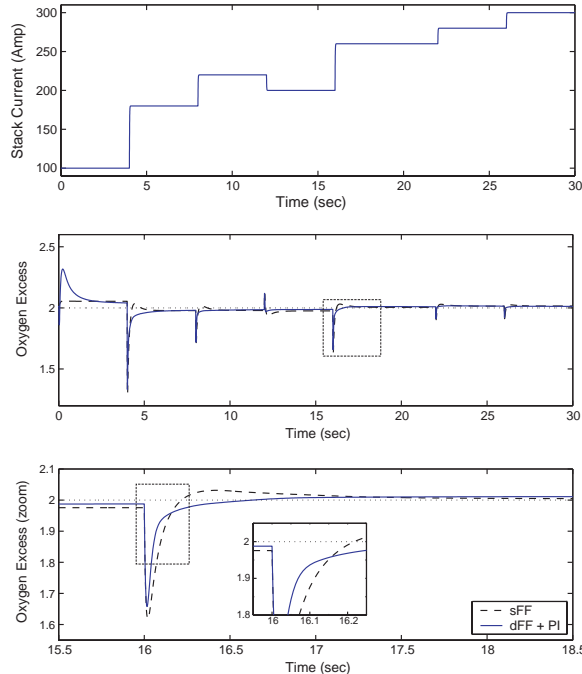

Fig. 9. Response of system with dynamic feedforward in nonlinear simulation

Figure 9 shows the response of the nonlinear system with the dFF+PI subjected to a series of current steps. The dFF+PI controller has a better disturbance rejection capability (from $w = I_{st}$ to $z_2 = \lambda_{O_2}$) than the one achieved with the static feedforward (sFF). After the initial excursion that cannot be avoided as long as a causal controller is implemented, the dFF+PI makes λ_{O_2} recover to the 0.2% band of the nominal λ_{O_2} within 0.04 sec, whereas the sFF makes λ_{O_2} recover within 0.075 sec. This shows that the dFF+PI system is approximately two times faster than the system with the static feedforward controller (sFF). Note also that the overshoot in $z_2 = \lambda_{O_2}$ for the case of the sFF controller is unfavorable since redundant power is used to produce this unnecessary overshoot. Moreover, the overshoot on the O_2 excess ratio is equivalent to O_2 starvation when the system is subjected to a step down disturbance.

The calibration and implementation of the PI controller is easy. But, the simplicity of this control configuration usually result in reduced system robustness (see Figure 13) as the control performance relies more on the feedforward path. In an effort to design a better (higher bandwidth) feedback controller, we explore next an observer-based feedback control design.

VII. Feedback Control Design

Well-designed feedback controllers have advantages over feedforward control in terms of robustness in the presence of unknown disturbance and plant parameter variations. The feedback controller is based on linear quadratic techniques decomposing the problem to a state feedback and an observer design using the separation principle. The linear model obtained from linearization with the static feedforward (sFF) is used in designing the feedback controller. See Appendix for specific values of the linear plant. Note here that we use the sFF and not the dFF in the linear model in order to keep the order of the observer-based feedback controller low.

A. State Feedback

The Linear Quadratic Regulator (LQR) algorithm is used to design the state feedback controller. Integral control can be used together with state feedback to reduce the steady-state error of the control output. Since the performance variable, λ_{O_2}, cannot be measured, integral control must be applied to one of the available measurements. The most obvious choice is assigning an integrator on the compressor flow rate, $y_1 = W_{cp}$, for two reasons: First, it is easy to measure W_{cp}. Second, it is relatively easy to calculate the required compressor air flow rate, $W_{cp}^* = f_{cp}(I_{st})$, that satisfies the desired oxygen excess ratio. This calculation (Eq. (27)) is based on electrochemical and thermodynamic calculations for known ambient conditions. The state equation of the integrator is thus

$$\dot{q} = W_{cp}^* - W_{cp} \tag{34}$$

The cost function

$$J = \int_0^\infty \delta\hat{x}^T C_{z2}^T Q_{z2} C_{z2} \delta\hat{x} + q^T Q_I q + \delta u^T R \delta u \, dt \tag{35}$$

is used for the state feedback

$$\delta u = -K \left[\delta\hat{x}, q\right]^T = -K_p \delta\hat{x} - K_I q \tag{36}$$

where the controller gain is $K := R^{-1}\hat{B}_u^T \bar{P}$ and $\bar{P}$ denotes the solution to the Algebraic Riccati Equation (ARE):

$$\bar{P}\hat{A} + \hat{A}^T \bar{P} + \hat{Q}_x - \bar{P}\hat{B}_u R^{-1} \hat{B}_u^T \bar{P} = 0 \tag{37}$$

where $\hat{A} = [A, 0 \; ; \; -C_{y1}, 0]$, $\hat{B}_u = [B_u; 0]$ $\hat{Q}_x = \text{diag}(Q_x, Q_I)$, $Q_x = C_{z2}^T Q_{z2} C_{z2}$.

The integral gain is set to small values due to the same reasons discussed in Section VI. Due to the fact that there is a disturbance feedthrough on the performance variable (see Eq. 28) we add a pre-compensator u_p from [12], [13], that modifies the control input u:

$$
\begin{aligned}
u &= u^* + u_p - K \left[\delta\hat{x}, q\right] \\
u_p &= \left[C_{z2}(A - B_u K_p)^{-1} B_u\right]^{-1} \left[D_{z2w} - C_{z2}(A - B_u K_p)^{-1} B_w\right]
\end{aligned} \tag{38}
$$

The linear responses of the system with full state feedback controller (u from Eq. (38)) and static feedforward ($u = u^*$) are shown in Figure 10. The response achieved with dynamic feedforward (dFF+PI) is practically

identical to the one achieved with the full state feedback controller (sFF+stateFB) so it is not shown. The response of the closed loop λ_{O_2} to I_{st} is twice faster than the open loop with the static feedforward (sFF). The closed loop transfer function from the disturbance $w = I_{st}$ to the performance variables $z_2 = \lambda_{O_2}$ is shown in Figure 11. It can be seen that both the dynamic feedforward based controller (dFF+PI) and the static feedforward with state feedback ("sFF+stateFB") reduce the magnitude of $z_2 = \lambda_{O_2}$ at frequencies between 0.5 and 40 rad/sec (0.08 to 6.4 Hz).
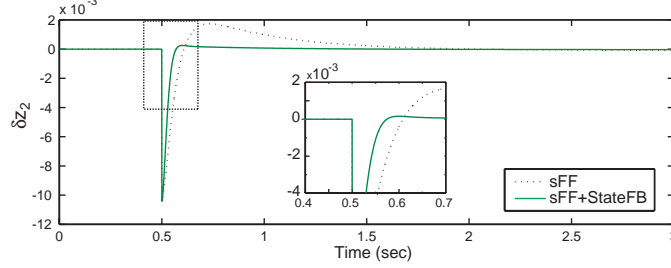

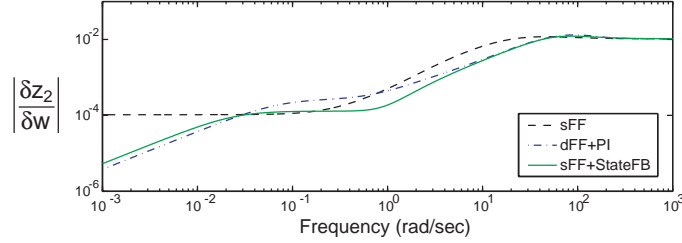Fig. 10.   Unit step response of system with full state feedback in linear simulation

Fig. 11.   Magnitude of frequency response of closed-loop system from w to z_2

In practice, to prevent stack starvation, the stack current signal is filtered by a low pass filter in order to allow enough time for the air supply system to increase air flow to the cathode. This solution, however, slows down the fuel cell power response because the power is a direct function of the current. Therefore, it is desirable to use the highest possible cutoff frequency in the low pass filter such that fast current can be drawn without starving the stack. As can be seen from Figure 11, to reduce the magnitude of the excess ratio, the current filter used for the controlled system can have higher cutoff frequency, which means that the controlled system can handle faster current drawn without starving the stack, and thus, faster power is produced from the fuel cell system.

B. Observer Design

The estimate of the state, $\delta\hat{x}$, used in the calculation of the control input (Eq. (38)) is determined using a state observer based on Kalman Filter design. Three measurements available are compressor air flow rate, $y_1 = W_{cp}$, supply manifold pressure, $y_2 = p_{sm}$, and fuel cell stack voltage, $y_3 = v_{st}$ (see Figure 2). These variables are relatively easy to measure. The compressor flow rate is typically measured for feedback to the compressor controller. The stack voltage is normally monitored for diagnostics and fault detection. Low voltage indicates a fault and triggers FCS shut-down and removes the current drawn from the FCS. The observer state equations are

$$
\begin{aligned}
\delta\dot{\hat{x}} &= A\delta\hat{x} + B_u\delta u + B_w^o\delta w + L(\delta y - \delta\hat{y}) \\
\delta\hat{y} &= C_y\delta\hat{x} + D_{yu}\delta u + D_{yw}\delta w
\end{aligned}
\tag{39}
$$

Based on the Linear Quadratic Gaussian method, the optimal observer gain, L, is

$$
L := SC_y^T W_y^{-1}
\tag{40}
$$

where S is the solution to

$$0 = SA^T + AS + V_x + SC_y^T W_y^{-1} C_y S \tag{41}$$

The positive definite matrices W_y and V_x represent the intensities of measurement noise and process disturbance, respectively [10].

TABLE I
EIGENVALUES, EIGENVECTORS, AND OBSERVABILITY

Eigenvalues								
λ	-219.63	-89.485	-46.177	-22.404	-18.258	-2.915	-1.6473	-1.4038
Eigenvectors								
x1	1.06E-16	-0.17539	-0.091325	3.43E-16	0.050201	0.024367	0.86107	-0.25619
x2	0.29428	0.016479	0.012583	0.1289	0.0036888	0.016047	0.007579	-0.0074482
x3	-3.23E-16	-0.74707	-0.099392	-5.92E-16	0.13993	0.44336	-0.14727	-0.098068
x4	-1.21E-16	-0.12878	-0.45231	3.24E-15	-0.98678	0.62473	0.27811	-0.27037
x5	-9.58E-18	0.0479	0.067229	-5.98E-17	0.0046179	0.046501	0.022519	-0.022231
x6	-7.23E-17	0.61398	0.86233	-7.93E-16	0.057898	0.6389	0.3981	-0.92234
x7	0.95572	0.071474	0.11197	-0.99166	-0.016026	-0.0078755	-0.0026628	0.0024275
x8	-3.04E-17	0.099469	-0.12794	-2.05E-16	0.022705	0.043444	0.021407	-0.019503
measuring y1								
rank(λI-A; C)	7	8	8	7	8	8	8	8
cond(λI-A; C)	1.29E+16	171.17	157.79	9.52E+16	461.59	1130.3	9728.4	2449.9
measuring y1 y2								
rank(λI-A; C)	7	8	8	7	8	8	8	8
cond(λI-A; C)	1.32E+16	171.16	157.79	3.15E+17	461.59	1130.3	9728.4	2449.9
measuring y1 y2 y3								
rank(λI-A; C)	8	8	8	8	8	8	8	8
cond(λI-A; C)	226.69	154.99	143.86	943.77	402.8	938.86	1617	1886.2

First, the analysis on observability could be performed using Table I, which shows the system eigenvalues, λ_i, the corresponding eigenvectors, and the corresponding rank and condition number of

$$\begin{bmatrix} \lambda_i I - A \\ C_y \end{bmatrix} \tag{42}$$

for three different cases: 1) measuring only y_1, 2) measuring y_1 and y_2, and 3) measuring all y_1, y_2, and y_3. The dynamics associated with an eigenvalue is unobservable if the corresponding matrix (42) loses rank (Section 2.4 of [20]). In this sense the corresponding eigenvalue can be called unobservable. A large condition number of a matrix implies that the matrix is almost rank deficient. Thus, the large condition number of the matrix (42) indicates a weakly observable eigenvalue λ_i.

Comparing cases 1 and 2, Table I shows that adding y_2 measurement does not change the observability. This is because pressure and flow are related with only an integrator. The eigenvalues -219.63 and -22.404 are not observable with measurements y_1 and y_2. The eigenvectors associated with these eigenvalues suggested that the unobservable mode is almost a representation of the mass of vapor in the anode, $m_{w,an}$. This agrees with the fact that the two measurements are in the air supply side and the only connection to the water in the anode is small membrane water flow. The hydrogen mass is however (more) observable through the anode flow control (which regulates anode pressure following cathode pressure). These two unobservable eigenvalues are however fast, and thus have small effect on observer performance. On the other hand, the slow eigenvalues at -1.6473 and -1.4038 can degrade observer performance because they are weakly observable, as indicated by large condition number at 9728.4 and 2449.9, respectively.

Adding the stack voltage measurement improves the state observability, as can be seen from the rank and the condition number for case 3. However, the high condition number for slow eigenvalue (-1.4038) could degrade observer performance. Many design iterations confirm the degradation. As when this eigenvalue is moved, the resulting observer gain is large, and thus producing large overshoot in observer error. From the implementation view point, when combined with a controller, large observer gain can produce a compensator with undesirably high gain. To prevent high observer gain, we design a reduced order output estimator

(closed-loop observer) for the observable part and an input estimator (open-loop observer) for the weakly observable part. Below, the design process for the case of three measurements is explained.

First, the system matrices are transformed to the modal canonical form $\delta\tilde{x} = T\delta x$ [7] such that the new system matrices are

$$\tilde{A} = TAT^{-1} = \begin{bmatrix} \lambda_1 & & 0 \\ & \ddots & \\ 0 & & \lambda_8 \end{bmatrix} \tag{43}$$

$$\tilde{C} = C_y T^{-1} \quad \tilde{B} = T \begin{bmatrix} B_w & B_u \end{bmatrix} \tag{44}$$

Note the special structure of matrix $\tilde{A}$ which has eigenvalues on the diagonal. The matrices are then partitioned into

$$\begin{bmatrix} \tilde{A}_o & 0 \\ 0 & \tilde{A}_{\bar{o}} \end{bmatrix}, \qquad \begin{bmatrix} \tilde{B}_o \\ \tilde{B}_{\bar{o}} \end{bmatrix}, \qquad \begin{bmatrix} \tilde{C}_o & \tilde{C}_{\bar{o}} \end{bmatrix} \tag{45}$$

where $\tilde{A}_{\bar{o}} = \lambda_8 = -1.4038$. The reduced-order observer gain, $\tilde{L}$, is then designed for matrices $\tilde{A}_o$, $\tilde{B}_o$, and $\tilde{C}_o$.

$$\tilde{L} := \tilde{S}\tilde{C}_o^T \tilde{W}_y^{-1} \tag{46}$$

$$0 = \tilde{S}\tilde{A}_o^T + \tilde{A}_o\tilde{S} + \tilde{V}_x + \tilde{S}\tilde{C}_o^T \tilde{W}_y^{-1}\tilde{C}_o\tilde{S}$$

The weighting matrices chosen are

$$\tilde{V}_x \quad = \quad \text{diag}[\ 0.01\ \ 10\ \ 10\ \ 0.01\ \ 10\ \ 10\ \ 10\ ] + \alpha\,\tilde{B}_o\,\tilde{B}_o^T \tag{47}$$

$$\tilde{W}_y \quad = \quad 1{\times}10^{-6}\ \text{diag}\begin{bmatrix} 10 & 100 & 1 \end{bmatrix} \tag{48}$$

which correspond to the process noise and to the measurement noise, respectively, in the stochastic Kalman estimator design [2]. The $\tilde{V}_x$ is in the form used in the feedback loop recovery procedure [10]. Using this procedure, the full state feedback loop gain properties can be recovered by increasing the value of α. The value of α chosen in this design is 30. The reduced-order observer gain, $\tilde{L}$, is then transformed to the original coordinate

$$L = T^{-1}\begin{bmatrix} \tilde{L} \\ 0 \end{bmatrix} \tag{49}$$

Figure 12 (right) shows the response of observer error based on three measurements in linear simulation. The initial errors of all states are set at 1% of maximum deviation from nominal point. It can be seen that most of the state converge within 0.4 seconds. There is one slow convergence which is caused by the weakly observable eigenvalue ($\lambda_8 = -1.4038$). Figure 12 (left) shows the observer response when using one measurement, $y_1 = W_{cp}$. Large overshoot and slow convergence can be observed.
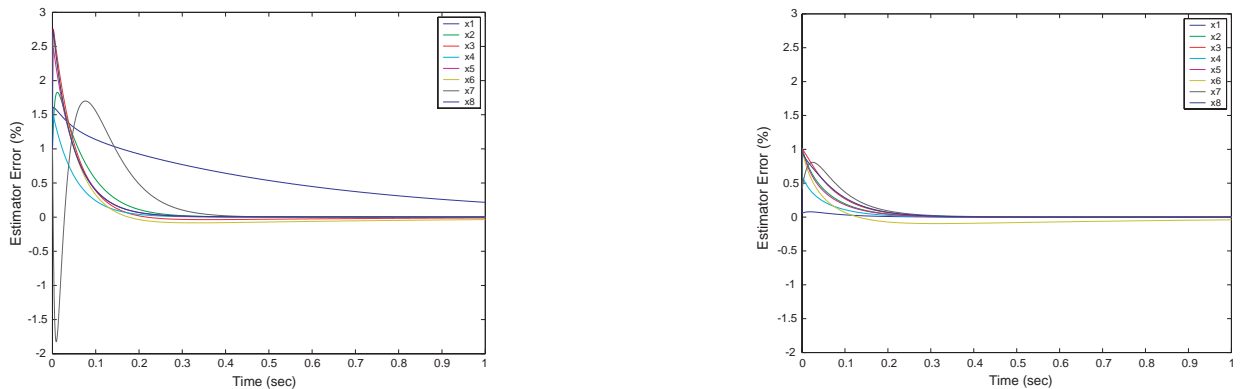

Fig. 12. Observer state error using only the first measurement (left) and all three measurements (right)

Figure 13 shows that the sFF+obsFB1 controller that is based on the single measurement $y_1 = W_{cp}$ cannot reduce the input sensitivity function as much as the sFF+obsFB3 controller can. The loop transfer recovery

method [10] could be used to bring the input sensitivity closer to that of full state feedback. However, the convergence rate of the observer becomes much slower. The sFF+obsFB1 controller has better bandwidth than the dFF+PI controller but the full potential of the model based controller is realized when the voltage measurement $y_3 = v_{st}$ is included in the feedback. In particular, Figure 13 shows that the sFF+obsFB3 fully recovers the full state feedback sensitivity.
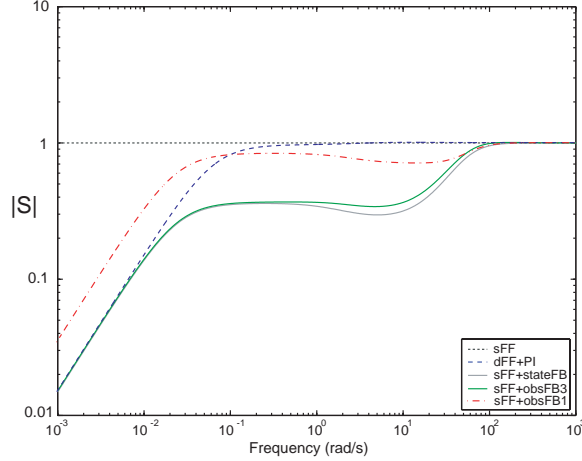

Fig. 13. Sensitivity function for different controllers

Simulations of the nonlinear system with different controllers are shown in Figure 14. Good transient response is achieved by both dynamic feedforward control (dFF+PI) and feedback control with three measurements (sFF+obsFB3). The feedback configuration is, however, superior in term of robustness. The analysis of the feedback controller performance and robustness indicates that the voltage measurement should be used as feedback to the controller and not only for safety monitoring.
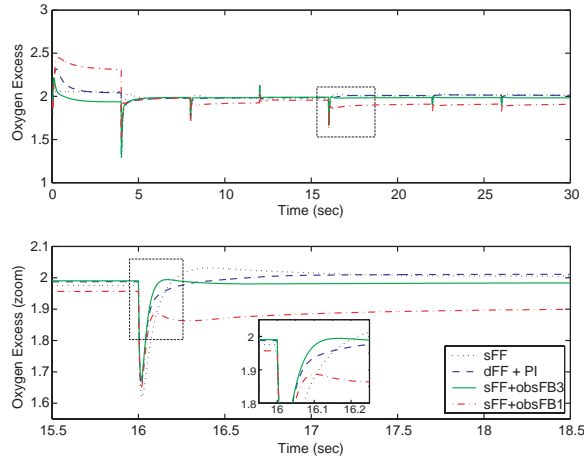

Fig. 14. Nonlinear simulation of system with different controllers

Different control configurations are considered in this first part of the paper. The control design and discussion of the features and properties of each control design are presented. The advantages and disadvantages, such as simplicity and robustness, of each configuration are succinctly explained. Because of its good performance and robustness, the observer-based feedback with the FCS voltage measurement is used in the remaining sections.

VIII. Closed Loop Fuel Cell Impedance

In this section we calculate the impedance of the closed loop fuel cell system comprised of (i) the air flow controller (sFF+obsFB3) with the observer-based feedback described above, (ii) the simple proportional anode

pressure controller, and (iii) the perfect cathode humidification incorporated in the model in Eq. (12) and (14). Figure 15 shows a schematic of the closed loop configuration with emphasis on the air flow controller. The closed loop FC system can now be viewed as a voltage source from the power management system.
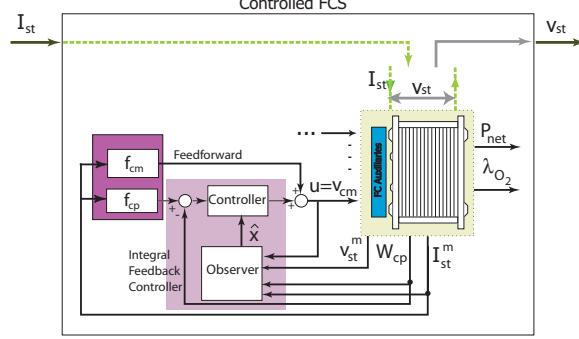

Fig. 15.   Controlled fuel cell stack as viewed from the power management system

The voltage of the controlled FCS (cFCS) can be written as $v_{st}(t) = v_{st}^o + \mathcal{L}^{-1}\left(Z_{cFCS}(s)\Delta I_{st}(s)\right)$ where $Z_{cFCS}(s)$ is the impedance of the cFCS and $\mathcal{L}$ is the Laplace transformation. Figure 16 shows the $Z_{cFCS}(s)$ in a Bode magnitude and phase plot. Electrochemical impedances are sometimes also shown with Nyquist plots (see for example [24], [38]) and used to identify the FCS performance for different material selection. The plot indicates that the cFCS can be represented by a passive resistance $\min\left(|Z_{cFCS}|\right) = R_{cFCS}^{min} = 0.05\ \Omega$ for current commands slower than 0.1 rad/sec. A passive resistance of $\max\left(|Z_{cFCS}|\right) \approx R_{cFCS}^{max} = 0.3\ \Omega$ can also be used for current commands faster than 100 rad/sec. From the phase of impedance $Z_{cFCS}(s)$, one can clearly see that the voltage drops for increasing current.
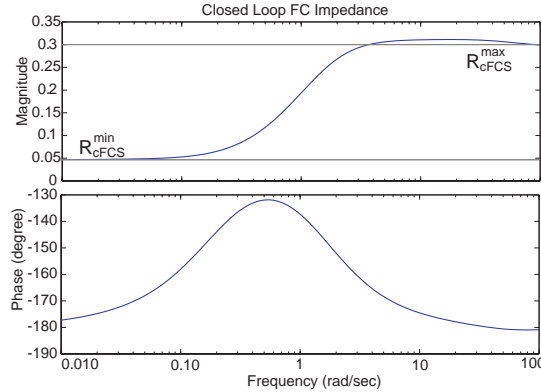

Fig. 16.   Impedance of the controlled fuel cell stack

A plot of current-voltage trajectories against non-controlled FCS polarization curves is shown in Figure 17. It is shown that immediately after a step change in current the voltage drops along the fixed cathode pressure polarization curve based on the high frequency impedance ($R_{cFCS}^{max} = 0.3\ \Omega$). After the initial transient, the controlled FCS shows a voltage that transverses to another polarization curve of higher cathode pressure. This behavior justifies the smaller cFCS resistance ($R_{cFCS}^{min} = 0.05\ \Omega$) at low frequencies. The increase in operating cathode pressure is dictated by the λ_{O_2} regulation. This phenomenon is associated with the high pressure air supply through a high speed compressor. A low pressure FCS will have similar controlled and uncontrolled impedances, primarily due to the approximately constant operating pressure.

IX. Tradeoff Between Two Performance Objectives

In the case when there is no additional energy storage device such as a battery or supercapacitor, the power used to run the compressor motor needs to be taken from the fuel cell stack. A transient step change in stack current requires rapid increase in air flow to prevent depletion of cathode oxygen. This requires a large
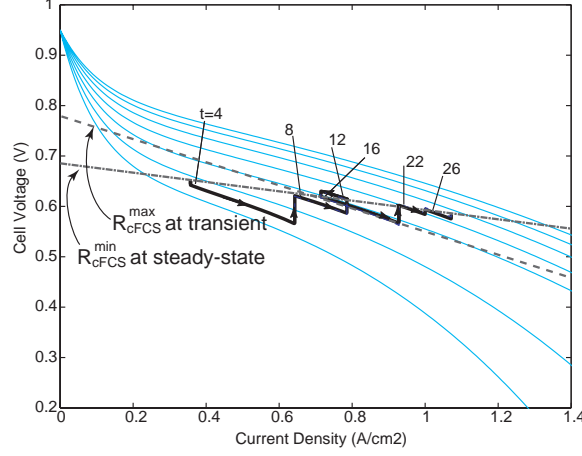
Fig. 17. Current-voltage trajectories that correspond to the nonlinear simulation of Figure 9

amount of power drawn by the compressor motor (P_{cm}) and thus increases parasitic loss, which affects the system net power $(P_{net} = P_{FC} - P_{cm})$.

The control problem that we have considered so far is the single-input single-output (SISO) problem of controlling the compressor command, $u = v_{cm}$, to regulate the oxygen excess ratio $z_2 = \lambda_{O_2}$. During steady-state, achieving the desired value of $z_2 = \lambda_{O_2}$ ensures that the desired net power $z_1 = P_{net}$ is obtained. During transient, however, the two objectives are independent, resulting in a Single-Input Two-Output (SITO) control problem [14] shown in Figure 18.
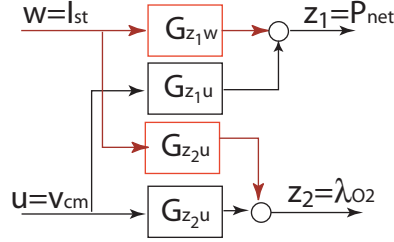

Fig. 18. Schematic of the coupling from I_{st} and v_{cm} to the performance variables P_{net} and λ_{O_2}.

Let us consider first the effects of the exogenous input $w = I_{st}$ and the control signal $u = v_{cm}$ on the first performance variable $z_1 = P_{net}(I_{st}, v_{cm}) = P_{FC}(I_{st}, v_{cm}) - P_{cm}(v_{cm})$, or in the linear sense $\delta z_1 = G_{z_1w} \cdot \delta w + G_{z_1u} \cdot \delta u$. As can be seen from the step responses in Figure 19, I_{st} has a positive effect on the net power. On the other hand, the compressor command, v_{cm}, causes an initial inverse response in the net power due to a non-minimum phase zero. The last plot in Figure 19 shows the net power during a step change in I_{st} together with a step change in $v_{cm} = f_{cm}(I_{st})$ that in steady-state ensures that $z_2 = \lambda_{O_2}^d = 2$. It can be seen that the time that is needed for P_{net} to reach the desired value is approximately one second.

It is apparent that to speed up the P_{net} response, we need either larger magnitude of I_{st} (to increase stack power) or smaller value of v_{cm} (to decrease the parasitic losses). Either case will degrade the speed of λ_{O_2} response because larger I_{st} causes additional drops in λ_{O_2} while smaller v_{cm} slows down the recovery rate of λ_{O_2}. The tradeoff between P_{net} and λ_{O_2} responses cannot be eliminated because there is only one control actuator. The actuator has to compromise between the two conflicting performance variables.

We systematically explore the tradeoff by setting up the LQ control problem with the cost function in terms of both performance variables:

$$J = \int_0^\infty Q_{z1}z_1^2 + Q_{z2}z_2^2 + Ru^2 + Q_I q^2 \, dt. \tag{50}$$

Figure 20 shows the time responses of the linear model with the different control gain based on different weighting in the cost function. The tradeoff between P_{net} and λ_{O_2} is evident during transient. In particular,
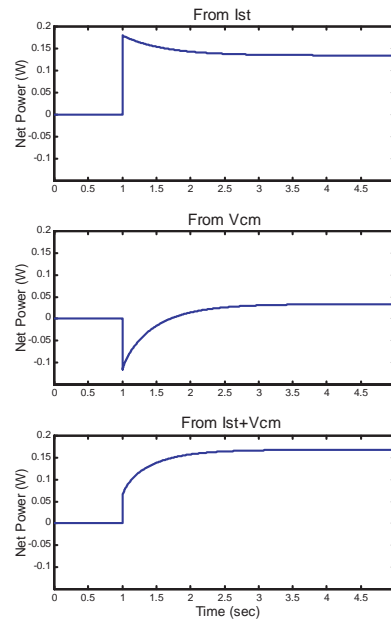
Fig. 19. Responses of P_{net} to steps in (i) I_{st}, (ii) v_{cm} and (iii) coordinated I_{st} and v_{cm}

controller design 4 (solid line) corresponds to the best power response but at the expense of slow recovery of the excess oxygen ratio. On the other hand, the fast recovery of excess oxygen ratio (dotted line) causes a net power lag of 0.200 sec which might be considered undesired.
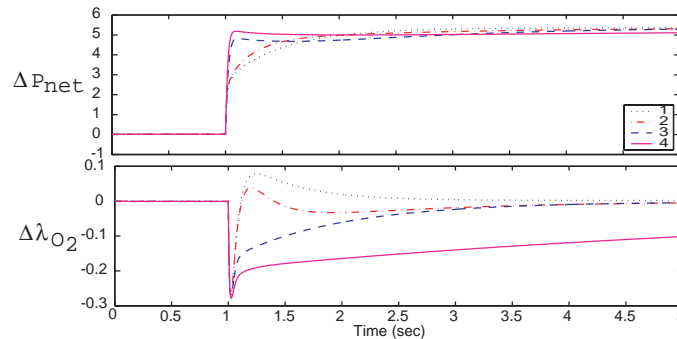

Fig. 20. Linear system response: 1 - feedforward 2 3 4 feedback with different gains

The same results are shown in the frequency domain using the Bode magnitude plots of Figure 21. The closer the two graphs are to zero, the better regulation is achieved. It can be seen that there is a severe tradeoff between the two variables in the frequency range between 0.7 rad/sec and 20 rad/sec. At these frequencies, when the magnitude of the upper variable is pushed closer to zero, the magnitude of the lower variable "pops up" indicating worse λ_{O_2} regulation. To decide for the best compromise between the two performance objectives, one needs to first establish a measure of how important to the stack life are the deviation in excess oxygen ratio.

One option to overcome the tradeoff is to filter the current drawn from the stack and to use an additional energy storage device (battery or ultra-capacitor) to supplement the system power during transient. Another option is to have an oxygen storage device placed near the entrance of the stack to provide an instant oxygen supply during rapid current changes. The required size of the energy or oxygen storage devices could be determined based on the frequencies associated with the tradeoff (Figures 11 and 21). The control analysis with the dynamics model of the fuel cell system provides an important tool to identify the required sizes (Amp-Hours) of these storage devices. Without this control analysis, it is very likely that unnecessary weight and volume are added to the FCS system by oversized auxiliary components.
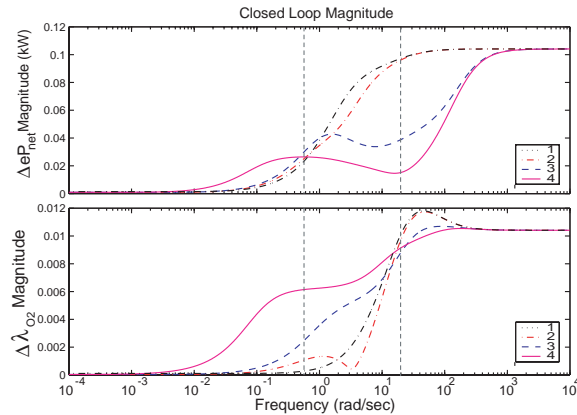
Fig. 21. Closed-loop frequency responses for different control gains.

X. Conclusions

In this paper we analyze and design air flow controllers that protect the FC stack from oxygen starvation during instantaneous step changes in current demand. The steady-state regulation of the oxygen excess ratio in the FCS cathode is achieved by assigning a slow integrator on the compressor flow. Linear observability techniques are employed to demonstrate the improvements of the transient oxygen regulation when the FCS voltage is included as measurement in the feedback controller. This is a measurement that until now has been used for diagnostics and emergency shut-down logic, so no extra cost is required. The FCS voltage signal contains high frequency information about the FC oxygen utilization and in hindsight of our design, it is a natural, and thus, powerful output for feedback.

We used linear optimal control design to identify the frequencies at which there is severe tradeoff between the transient system net power performance and the stack starvation control. The limitation arises when the FCS system architecture dictates that all auxiliary equipments are powered directly from the fuel cell with no secondary power sources. This plant configuration is preferred due to its simplicity, compactness and low cost. The result can be used to define the cutoff frequency for a filter that limits the current drawn from the fuel cell.

The closed loop current-voltage dynamic relationship is finally captured by the FCS impedance. We expect that the derived closed-loop FCS impedance will provide the basis for a systematic design of fuel cell stack electronic components.

In the future we will evaluate the air flow controller under uncertain conditions in the cathode air and membrane humidity. Moreover, we will evaluate our homogeneity assumption by studying the effect of the spatial variations in the gas concentration across the flow field.

APPENDIX

TABLE II
LINEARIZATION RESULTS WITHOUT STATIC FEEDFORWARD

A

-6.30908	0	-10.9544	0	83.74458	0	0	24.05866
0	-161.083	0	0	51.52923	0	-18.0261	0
-18.7858	0	-46.3136	0	275.6592	0	0	158.3741
0	0	0	-17.3506	193.9373	0	0	0
1.299576	0	2.969317	0.3977	-38.7024	0.105748	0	0
16.64244	0	38.02522	5.066579	-479.384	0	0	0
0	-450.386	0	0	142.2084	0	-80.9472	0
2.02257	0	4.621237	0	0	0	0	-51.2108

B_u

0
0
0
3.946683
0
0
0
0

B_w

-0.03159
-0.00398
0
0
0
0
-0.05242
0

C_z

-2.48373	-1.9773	0.109013	-0.21897	0	0	0	0
-0.63477	0	-1.45035	0	13.84308	0	0	0

D_{zu}

0.169141
0

D_{zw}

-0.0108
-0.01041

C_y

0	0	0	5.066579	-116.446	0	0	0
0	0	0	0	1	0	0	0
12.96989	10.32532	-0.56926	0	0	0	0	0

D_{yu}

0
0
0

D_{yw}

0
0
-0.29656

TABLE III
LINEARIZATION RESULTS INCLUDING STATIC FEEDFORWARD

A

-6.30908	0	-10.9544	0	83.74458	0	0	24.05866
0	-161.083	0	0	51.52923	0	-18.0261	0
-18.7858	0	-46.3136	0	275.6592	0	0	158.3741
0	0	0	-17.3506	193.9373	0	0	0
1.299576	0	2.969317	0.3977	-38.7024	0.105748	0	0
16.64244	0	38.02522	5.066579	-479.384	0	0	0
0	-450.386	0	0	142.2084	0	-80.9472	0
2.02257	0	4.621237	0	0	0	0	-51.2108

B_u

0
0
0
3.942897
0
0
0
0

B_w

-0.03159
-0.00398
0
2.681436
0
0
-0.05242
0

C_z

-2.48373	-1.9773	0.109013	-0.21897	0	0	0	0
-0.63477	0	-1.45035	0	13.84308	0	0	0

D_{zu}

0.168979
0

D_{zw}

0.104116
-0.01041

C_y

0	0	0	5.066579	-116.446	0	0	0
0	0	0	0	1	0	0	0
12.96989	10.32532	-0.56926	0	0	0	0	0

D_{yu}

0
0
0

D_{yw}

0
0
-0.29656

REFERENCES

[1] J.A. Adams, W-C Yang, K.A. Oglesby, and K.D. Osborne. The development of Ford's P2000 fuel cell vehicle. *SAE Paper 2000-01-1061*.

[2] Brian D. O. Anderson and John B. Moore. *Optimal Control: Linear Quadratic Methods*. Prentice-Hall, New Jersey, 1989.

[3] A.J. Appleby. The electrochemical engine for vehicles. *Scientific American*, pages 74–79, July 1999.

[4] M. Arcak, H. Gorgun, L.M. Pedersen, and S. Varigonda. An adaptive observer design for fuel cell hydrogen estimation. *to be presented in 2003 American Control Conference*, 2003.

[5] M. D. Di Benedetto and P. Lucibello. Inversion of nonlinear time-varying systems. *IEEE Transactions on Automatic Control*, 38(8):1259–1264, 1993.

[6] D.D. Boettner, G. Paganelli, Y.G. Guezennec, G. Rizzoni, and M.J. Moran. On-board reforming effects on the performance of proton exchange membrane (PEM) fuel cell vehicles. *Journal of Energy Resources Technology, Transactions of the ASME*, 124(3):191–196, 2002.

[7] Chi-Tsong Chen. *Linear System Theory and Design*. Oxford University Press, New York, 1998.

[8] S. Devasia. Should model-based inverse inputs be used as feedforward under plant uncertainty? *IEEE Transactions on Automatic Control*, 41(11):1865–1871, 2002.

[9] S. Devasia, D. Chen, and B. Paden. Nonlinear inversion-based output tracking. *IEEE Transactions on Automatic Control*, 41(7):930–942, 1996.

[10] J. C. Doyle and G. Stein. Robustness with observers. *Transactions on Automatic Control*, AC-24(4):607–611, 1979.

[11] B.A. Francis and W.M. Wonham. The internal model principle of control theory. *Automatica*, 12(5):457–465, 1976.

[12] Gene F. Franklin, J. David Powell, and Abbas Emani-Naeini. *Feedback Control of Dynamic Systems*. Addison-Wesley, New York, 1994.

[13] J. Freudenberg. A first graduate course in feedback control, 2002. University of Michigan, EECS 565 Coursepack.

[14] J. Freudenberg and R. Middleton. Properties of single input, two output feedback systems. *International Journal of Control*, 72(16):1446–1465, 1999.

[15] R.S. Glass. Sensor needs and requirements for fuel cells and CIDI/SIDI engines. Technical report, Department of Energy, April 2000. Published by Lawrence Livermore National Laboratory.

[16] W.R. Grove. A gaseous voltaic battery. *Philosophical Magazine*, 21:417–420, 1842.

[17] L. Guzzella. Control oriented modelling of fuel-cell based vehicles. *Presentation in NSF Workshop on the Integration of Modeling and Control for Automotive Systems*, 1999.

[18] W.W. Jacques. Electricity direct from coal. *Harper's Magazine*, 94:144–150, 1896.

[19] K. Jost. Fuel-cell concepts and technology. *Automotive Engineering International*, March 2000.

[20] Thomas Kailath. *Linear Systems*. Prentice-Hall, New Jersey, 1980.

[21] L.E. Lesster. Fuel cell power electronics: Managing a variable-voltage DC source in a fixed-voltage AC world. *Fuel Cells Bulletin*, 2(25):5–9, 2000.

[22] T.V. Nguyen and R.E. White. A water and heat management model for proton-exchange-membrane fuel cells. *Journal of Electrochemical Society*, 140(8):2178–2186, 1993.

[23] J. Padulles, G.W. Ault, C.A. Smith, and J.R. McDonald. Fuel cell plant dynamic modelling for power systems simulation. *Proceedings of 34th Universities Power Engineering Conference*, 34(1):21–25, 1999.

[24] V.A. Paganin, C.L.F. Oliveira, E.A. Ticianelli, T.E. Springer, and E.R. Gonzalez. Modelistic interpretation of the impedance response of a polymer electrolyte fuel cell. *Electrochimica Acta*, 43(24):3761–3766, 1998.

[25] F. Panik. Fuel cells for vehicle applications in cars - bringing the future closer. *Journal of Power Sources*, 71:36–38, 1998.

[26] S. Pischinger, C. Schönfelder, W. Bornscheuer, H. Kindl, and A. Wiartalla. Integrated air supply and humidification concepts for fuel cell systems. *SAE Paper 2001-01-0233*.

[27] Jay Tawee Pukrushpan. *Modeling and Control of Fuel Cell Systems and Fuel Processors*. PhD thesis, University of Michigan, 2003.

[28] J.T. Pukrushpan, H.Peng, and A.G. Stefanopoulou. Modeling and analysis of fuel cell reactant flow for automotive applications. *submitted to Journal of Dynamic Systems, Measurement, and Control*.

[29] J.T. Pukrushpan, H. Peng, and A.G. Stefanopoulou. Simulation and analysis of transient fuel cell system performance based on a dynamic reactant flow model. *Proceedings of the ASME International Mechanical Engineering Congress & Exposition*, 2002.

[30] J.T. Pukrushpan, A.G. Stefanopoulou, S. Varigonda, L.M. Pedersen, S. Ghosh, and H. Peng. Control of natural gas catalytic partial oxidation for hydrogen generation in fuel cell applications. *to be presented in 2003 American Control Conference*, 2003.

[31] K. Rajashekara. Propulsion system strategies for fuel cell vehicles. *SAE Paper 2000-01-0369*.

[32] K. Ro and S. Rahman. Control of grid-connected fuel cell plants for enhancement of power system stability. *Renewable Energy*, 28:397–407, 2003.

[33] C.F. Schœnbein. The voltaic polarization of certain solid and fluid substances. *Philosophical Magazine*, 14:43–45, 1839.

[34] T.E. Springer, R. Rockward, T.A. Zawodzinski, and S. Gottesfeld. Model for polymer electrolyte fuel cell operation on reformate feed. *Journal of The Electrochemical Society*, 148:A11–A23, 2001.

[35] T.E. Springer, T.A. Zawodzinski, and S. Gottesfeld. Polymer electrolyte fuel cell model. *Journal of Electrochemical Society*, 138(8):2334–2342, 1991.

[36] B. Thorstensen. A parametric study of fuel cell system efficiency under full and part load operation. *Journal of Power Sources*, 92:9–16, 2001.

[37] S. Varigonda, J.T. Pukrushpan, and A.G. Stefanopoulou. Challenges in fuel cell power plant control: The role of system level dynamic models. *AIChE Spring Meeting*, 2003.

[38] N. Wagner, W. Schnurnberger, B. Muller, and M. Lang. Electrochemical impedance spectra of solid-oxide fuel cells and polymer membrane fuel cells. *Electrochimica Acta*, 43(24):3785–3793, 1998.

[39] W-C Yang, B. Bates, N. Fletcher, and R. Pow. Control challenges and methodologies in fuel cell vehicle development. *SAE Paper 98C054*.